IOP Publishing Biomed. Mater. 19 (2024) 055043 https://doi.org/10.1088/1748-605X/ad7085

Biomedical Materials

PAPER

Effect of hematoma on early degradation behavior of magnesium after implantation

Yu Yusa[1,*], Yoshinaka Shimizu[1,2], Masanobu Hayashi[1], Takayuki Aizawa[1], Takahiro Nakahara[2], Takahiro Ueno[2], Akimitsu Sato[1], Chieko Miura[1], Akiko Yamamoto[3] and Yoshimichi Imai[1]

[1] Department of Plastic and Reconstructive Surgery, Tohoku University Graduate School of Medicine, 2-1 Seiryo-machi, Aoba-ku, Sendai, Miyagi 980-8575, Japan
[2] Central Research Laboratories, Nihon Parkerizing Co., Ltd, 4-5-1 Ohkami, Hiratsuka, Kanagawa 254-0012, Japan
[3] Research Center for Functional Materials, National Institute for Materials Sciences, 1-1 Namiki, Tsukuba, Ibaraki 305-0044, Japan
[*] Author to whom any correspondence should be addressed.

E-mail: yusayu.yusayu@gmail.com

Keywords: magnesium, hematoma, Raman analysis, energy-dispersive x-ray spectroscopy, insoluble salt

Supplementary material for this article is available online

OPEN ACCESS

RECEIVED
1 May 2024

REVISED
25 June 2024

ACCEPTED FOR PUBLICATION
16 August 2024

PUBLISHED
27 August 2024

Abstract

The corrosion of magnesium (Mg)-based bioabsorbable implanting devices is influenced by implantation environment which dynamically changes by biological response including wound healing. Understanding the corrosion mechanisms along the healing process is essential for the development of Mg-based devices. In this study, a hematoma model was created in a rat femur to analyze Mg corrosion with hematoma in the early stage of implantation. Pure Mg specimen (99.9%, $\varphi 1.2 \times 6$ mm) was implanted in rat femur under either hematoma or non-hematoma conditions. After a designated period of implantation, the specimens were collected and weighed. The insoluble salts formed on the specimen surfaces were analyzed using scanning electron microscopy, energy-dispersive x-ray spectroscopy, and Raman spectroscopy on days 1, 3, and 7. The results indicate that hematomas promote Mg corrosion and change the insoluble salt precipitation. The weight loss of the hematoma group (27.31 ± 5.91 μg mm^{-2}) was significantly larger than that of the non-hematoma group (14.77 ± 3.28 μg mm^{-2}) on day 7. In the non-hematoma group, carbonate and phosphate were detected even on day 1, but the only latter was detected on day 7. In the hematoma group, hydroxide was detected on day 1, followed by the formation of carbonate and phosphate on days 3 and 7. The obtained results suggest the hypoxic and acidic microenvironment in hematomas accelerates the Mg corrosion immediately after implantation, and the subsequent hematoma resorption process leads to the formation of phosphate and carbonate with organic molecules. This study revealed the risk of hematomas as an acceleration factor of the corrosion of Mg-based devices leading to the early implant failure. It is important to consider this risk in the design of Mg-based devices and to optimize surgical procedures controlling hemorrhage at implantation and reducing unexpected bleeding after surgery.

1. Introduction

Biomedical application of magnesium (Mg) alloys as fracture fixation devices has been researched worldwide [1, 2]. Because Mg alloys have bioabsorbability and adequate strength, their biomedical application in orthopedic and maxillofacial areas will change the design and function of existing osteosynthesis implants, replacing conventional Ti and absorbable polymers [2–4]. However, Mg alloys react with water immediately after implantation; the highest corrosion rate is generally observed immediately after the implantation [5]. The corrosion of Mg alloys depends on the surrounding environment, especially the pH of the electrolyte [6–9].

Mg corrosion in the simulated body fluid results in the releases of Mg ions (Mg^{2+}), hydroxide ions (OH^-), and hydrogen (H_2) gas. The corrosion of Mg are described by the following reactions [3, 10]

$$Mg \rightarrow Mg^{2+} + 2e^{-}\ (\text{anodic reaction}) \ldots \quad (1)$$

$$2H_2O + 2e^{-} \rightarrow H_2 + 2OH^{-}\ (\text{cathodic reaction}) \ldots \quad (2)$$

$$Mg + 2H_2O \rightarrow Mg^{2+} + 2OH^{-} + H_2\ (\text{overall reaction}) \ldots. \quad (3)$$

The released OH^{-} ions increase the pH of the electrolyte surrounding the Mg specimen [11, 12] and causes the precipitation of insoluble salts such as hydroxide, carbonate, and phosphate [12, 13]. In case of a simple simulated body fluid such as 0.9% NaCl, which has a limited buffering capacity, $Mg(OH)_2$ is precipitated on the Mg surface. However, it is converted to highly water-soluble $MgCl_2$ by chloride ions (Cl^{-}) by the following reaction [14].

$$Mg(OH)_2 + 2Cl^{-} \rightarrow MgCl_2 + 2OH^{-} \ldots. \quad (4)$$

Since body fluids contain calcium and phosphate ions, the precipitation of calcium phosphate on the specimen surface is reported [10]. The formation of an insoluble salt layer on the specimen surface hindered the contact of water molecule to the Mg metal substrate, resulting in the retardation of the corrosion.

As in the above reaction (3), the H_2 generation rate is proportional to the Mg corrosion rate; it also decreases with increase in insoluble salt precipitation. The released ions and generated H_2 diffuse into the tissue by dissolving into the body fluid and capillary flow. When the H_2 generation is larger than H_2 diffusion, the gas cavity is formed in the tissue [15]. Subsequently, the H_2 generation decreases and capillary grows, which gradually results in the reduction of gas cavity volume in the tissue.

The corrosion of the implanted Mg alloys is susceptible for complex physiological environment influenced by implantation site, ionic concentration, and diffusion capacity of the surrounding tissue [16]. It is further complicated by the action of cells in wound and fracture healing at the implantation site, which induces the dynamic changes in the circulatory environment due to angiogenesis and granulation [17]. Surgical intervention and bleeding at fracture sites can also be one of the influencing factors; a certain amount of hemorrhage forms a hematoma, which generates a hypoxic microenvironment inducing anaerobic metabolism resulting in lactic acid production and an acidic environment [18–20]. This environment becomes even more acidic by osteoclasts activities [21]. Moreover, an acidic environment at the fracture site induces resorption of hydroxyapatite from the bone, which increases calcium and phosphate ions in the body fluids [18].

In clinical cases of fracture fixation, the hematoma formation occurs at a certain rate due to insufficient hemostatic technique and unexpected bleeding [22]. It may also be influenced by the fracture conditions and patient underlying disease. Unexpected bleeding is not considered to cause a serious damage on conventional, non-absorbable metal fixtures, however, no information is available for Mg-based, bioabsorbable fixtures. Clinically available Mg-based device is suspected to cause complications such as infection and osteolysis in about 13.3% of cases, which remains a problem that must be solved [15, 23, 24].

It is mandatory for Mg-based devices to control their corrosion to achieve the clinical success. Analysis of the corrosion mechanism of Mg in the early implantation phases is essential for better control of its corrosion behavior in physiological environment. As most implantation studies were performed in normal tissues, such as marrow cavity, or intramuscular tissue adjacent to bone [25–27], the effects of hematoma on Mg corrosion remain unclear. A few *in vitro* studies reported the higher Mg^{2+} release from the Mg alloys in contact to whole blood for 6 h than in PBS(-) or plasma [28, 29]. However, no report describes the detailed relationship between Mg corrosion behavior and hematoma within one week of implantation *in vivo* with detailed analysis of the insoluble salts formed on the specimen surface.

This study aims to analyze the effect of hematoma on Mg corrosion and insoluble salt precipitation in the early phase of implantation. Through the study, we can obtain useful and unprecedented knowledge on the mechanism of Mg corrosion *in vivo*, which will contribute to the development and improvement of the quality of Mg-based devices for fracture fixation.

2. Methods

2.1. Test materials

Commercially available pure Mg wire (99.9%, φ1.2 mm, MACRW Co., Ltd, Shizuoka, Japan) was cut into 6 mm lengths and both ends were polished with JIS #2500 using a SiC paper. The nominal compositions of the Mg wires are listed in table 1. The natural oxide film on the specimen surface was removed by immersion into a nital solution (5% nitric acid in ethanol) at 20 °C in an ultrasonic cleaner, and the specimen was washed with ultrapure water before drying under vacuum [30, 31]. The pretest weight of each specimen (W_0 [mg]) was measured using an electronic balance (BM-5; A&D Corporation, Tokyo, Japan). The specimen length was decided based on the W_0, specimen radius (0.6 [mm]), and the density of pure Mg (1.738 [mg mm^{-3}]) as

Table 1. Composition of the pure Mg wire (mass%).

	Al	Mn	Zn	Si	Cu	Ni	Fe	Mg
pure Mg (99.9%)	0.009	0.011	0.016	0.003	0.008	0.001	0.002	Bal.

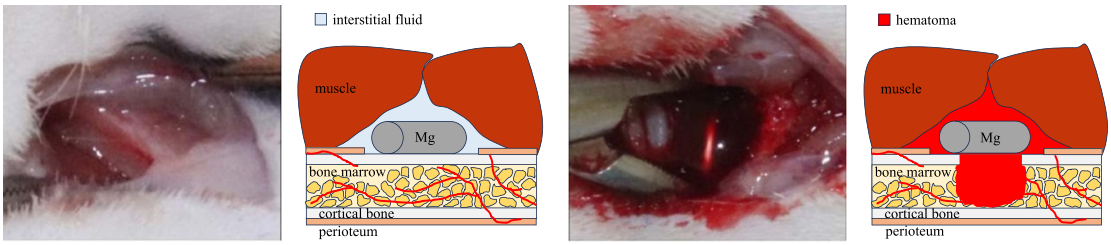

Figure 1. Sample placement in rat femur. Non-hematoma group (left) and hematoma group (right).

$W_0/(\pi \times 0.6^2 \times 1.738)$, which giving the initial surface area of the specimen (S_0 [mm^2]) by equation (1),

$$S_0 = 2 \times 0.6 \times 0.6 \times \pi + \frac{2 \times W_0}{0.6 \times 1.738}. \quad (1)$$

2.2. Implantation in rats

The animal experimental protocol was reviewed and approved by the Animal Care and Use Committee of Tohoku University (Sendai, Japan, approval number: 2022MdA-009-01). It follows the Guide for the Care and Use of Laboratory Animals, 8th ed. (National Research Council, revised in 2010). Eleven-week-old Wistar rats were purchased and acclimatized with normal feed and tap water for one week. Six twelve-week-old rats (mean weight: 272 ± 10.4 [mg]) were assigned to each of implantation periods (1, 3, 7 d) and implantation surgery was performed. Three additional animals per each implantation period were subjected to implantation for analysis by scanning electron microscopy (SEM) and Raman spectroscopy.

2.3. Implantation procedure

General anesthesia was induced by inhalation of 5.0% isoflurane (isoflurane for animals, Intervet, Tokyo, Japan), and the concentration of isoflurane was maintained at 2.5 [vol.%] intraoperatively. Local anesthesia was performed by subcutaneous injection of 1% lidocaine with epinephrine (<0.01 mg kg^{-1}; Xylocaine®□ injection 1% epinephrine, AstraZeneca, Osaka) in the middle thigh. A 1 cm long skin incision was made in the middle of the thigh followed by careful dissection of the intermuscular space approaching to the femur mind avoiding unnecessary bleeding. The group without hemorrhage from the femoral bone marrow was defined as the non-hematoma group (figure 1, left). In the other group, after a femoral approach was prepared by the same manner to the non-hematoma group, a hole of 1.6 mm diameter was drilled by a steel bar (ST1 HP 016, Hager & Meisinger GmbH, Germany) in the anterior aspect of the femur to create a hematoma. Then, the implantation space of approximately 4–5 mm wide, 8–10 mm long, and 3–4 mm in depth was filled with approximately 200 mm^3 of hematoma, and the entire specimen was inserted in the hematoma. The group with this bone hole was defined as the hematoma group (figure 1, right). After insertion of the specimen, the fascia was closed using nylon thread to prevent the specimen from displacement, and the wound was closed with skin sutures.

Every rat received 2 specimens; 1 on its left femur for the hematoma condition and 1 on its right for the non-hematoma condition. For the weight loss and insoluble salt quantification, 6 specimens are used per group per implantation period. For the scanning electron microscope equipped with an energy-dispersive x-ray spectrometer (SEM-EDX) and Raman spectroscopy, 3 specimens were employed per group per implantation period. The weights of the specimens from the non-hematoma and hematoma groups were 10.678 ± 0.085 mg and 10.843 ± 0.073 mg respectively.

After implantation, the experimental animals were kept individually in cages; there was no significant weight loss in all animals. No signs of infection such as wound dehiscence or drainage were identified in all cases, although no antibiotics were administered. The animals were euthanized to collect the specimen for analysis on days 1, 3, and 7. At the time of specimen collection, all specimens were in contact with the femur. Collected specimens were vacuum bagged to prevent oxidation and stored in vacuum desiccators.

2.4. Specimen weight measurement

The specimens were collected and washed with ultrapure water before vacuum drying. The weight of the specimen after implantation (W_1 [mg]) was measured to calculate the weight of insoluble salt

per unit surface area (W_{inso} [mg mm^{-2}]) using equation (2),

$$W_{inso} = \frac{W_1 - W_0}{S_0}. \quad (2)$$

Each of the six specimens per group per implantation period was immersed in 5 mL of a chromic acid mixture (20 g of CrO_3, 1 g of $AgNO_3$, and 2 g of $Ba(NO_3)_2$ in 100 ml distilled water) to remove the insoluble salts and rewashed with ultrapure water before vacuum drying. The chromic acid mixture after specimen immersion was collected for further analysis (section 2.5).

The weight (W_r [mg]) of each specimen after chromic acid cleaning was measured to calculate the weight loss per unit surface area (W_{loss} [mg mm^{-2}]) using equation (3),

$$W_{loss} = \frac{W_0 - W_r}{S_0}. \quad (3)$$

2.5. Quantitative analysis of insoluble salts

Mg, calcium (Ca), and phosphorus (P) in the collected acid mixture were quantitatively analyzed using inductively coupled plasma-mass spectrometry (ICP-MS). The difference between the elemental concentration in the collected chromic acid mixture (C_{cp} [μg mL^{-1}]) and that in the unused acid mixture ($C_{control}$ [μg ml^{-1}]) gave the amount in precipitation per unit surface area W_{cp} [mg mm^{-2}] using equation (4),

$$W_{cp} = \frac{(C_{cp} - C_{control}) \times 5}{1000 \times S_0}. \quad (4)$$

2.6. Analysis of insoluble salts by SEM-EDX

The surface of the post-implantation specimens was analyzed using a SEM-EDX (S-4800, Hitachi High-Technologies Corporation, Tokyo, Japan). Prior to the SEM observation, the specimen surface was coated with platinum. Elemental analysis was performed at an acceleration voltage of 15 keV and resolution of 512 × 384 [pixels]. The percentage elemental distribution of Mg, Ca, P, carbon (C), and oxygen (O) was analyzed on the surface of three post-implantation specimens per group.

2.7. Analysis of insoluble salts using micro-Raman spectroscopy

The post-implantation specimens were analyzed by Raman spectroscopy (Laser Raman Spectrophotometer Automatic Imaging System NRS-5100; Japan Spectroscopy Corporation, Tokyo, Japan). One or two typical places on the surface were analyzed per specimen. The measurement conditions were as follows; grating L = 600 nm, B = 500 nm, objective lens magnification = 100, excitation laser = 532.13 nm, exposure time = 10 s, number of integrations = 5 times, laser power = 3.2 mW (50% in measurement), and wave number range = 100–3700 cm^{-1}.

2.8. Statistical processing

All data are presented as mean ± standard deviation. Statistical analysis of group differences was performed using JSTAT 6.9 for windows, with t-test and linear regression analysis.

3. Results

3.1. Weight loss of magnesium specimen

The weight loss of the specimens was summarized in figure 2(a) and table S1 in the supplementary materials. As shown in figure 2(a), the weight loss of both groups increased depending on the square root of the implantation period, indicating a decrease in the weight loss per day with an increase in the implantation period. The increasing trend of the weight loss (i.e. the slope of the regression line against the square root of the implantation period) of the hematoma group is twice as large as that of the non-hematoma group ($p < 0.01$ by the parallelism test of 2 regression lines). This suggests the involvement of diffusion process on the corrosion rate of the Mg specimen. After 7 d of implantation, the average weight loss of the hematoma group was 27.31 ± 5.91 μg mm^{-2}, which was 1.8 times larger than that of the non-hematoma group (14.77 ± 3.28 μg mm^{-2}). Chen *et al* reported the weight loss rate of pure Mg specimens (1.1 mmφ × 15 mm) implanted into rabbit muscle tissue for 1 week was 4.7% [32], which equals to 21.58 μg mm^{-2}. This value is slightly larger than that of the non-hematoma group, probably due to the differences in the implantation tissue, animal species, specimen size and impurities.

3.2. Weight of insoluble salts

The weight of the insoluble salts was summarized in figure 2(b) and table S2 in the supplementary materials. The parallelism test of the regression lines for both hematoma and non-hematoma groups against the square root of the implantation period indicates a significant difference not in the increasing rate of the insoluble salt weight (i.e. a slope of the regression line) but in the initial weight of the insoluble salts (i.e. a intercept of the regression line, $p < 0.01$). This suggests that the specimens in the hematoma group have significantly larger amount of salt precipitation in the very early stage of the implantation (within 24 h).

In figure 2(c), W_{inso}/W_{loss} was plotted against the square root of the implantation period, indicating the clear difference between hematoma and non-hematoma groups. For the latter group, it was stable at around 0.9, whereas that for the hematoma group decreased with an increase in the implantation period. The higher W_{inso}/W_{loss} ratio indicates more precipitation of insoluble salts. This can be achieved

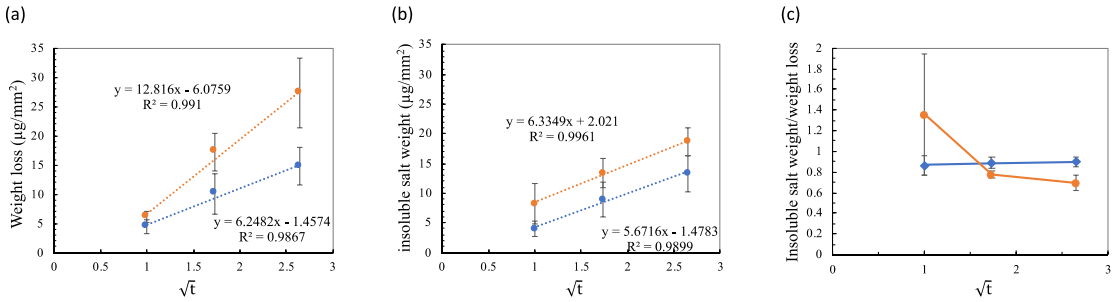

Figure 2. Results of (a) weight loss per unit surface area, (b) weight of insoluble salts formed on the specimen surface after implantation, and (c) ratios of insoluble salt weight to weight loss plotted against the square root of the implantation period, $\sqrt{t}$. In (a), the increasing trend in the weight loss of the hematoma group is significantly larger than that of non-hematoma group ($p < 0.05$ by the parallelism test of 2 regression lines). In (b), there is no significant difference in the increasing trends of the insoluble salt weight between the hematoma and non-hematoma groups, but their intercepts (the initial insoluble salt weight) are significantly different ($p < 0.01$ by the parallelism test of 2 regression lines).

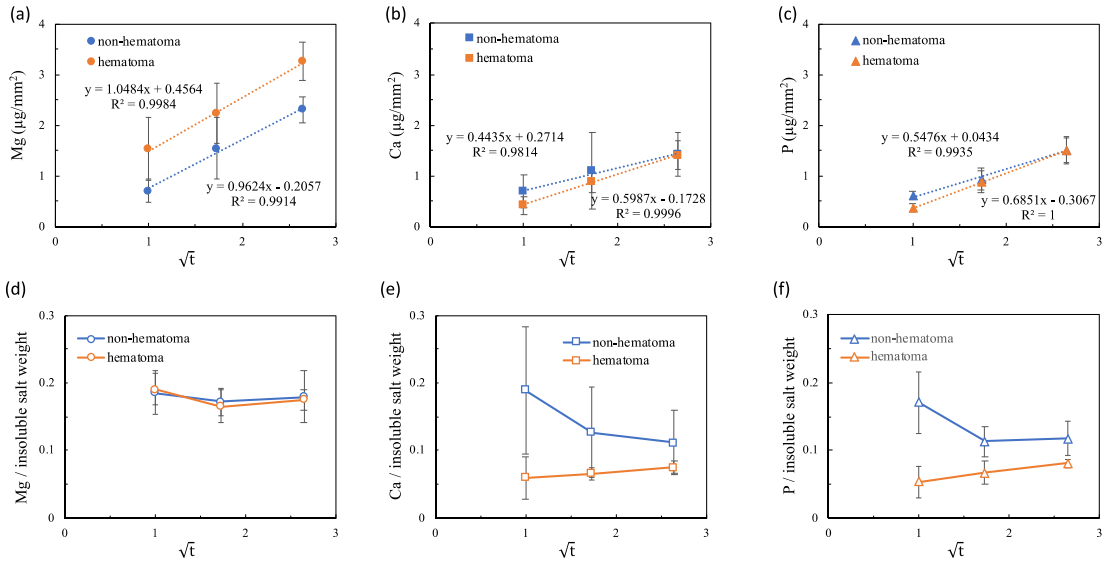

Figure 3. Results on quantification of Mg (a), Ca (b), and P (c) in insoluble salt on days 1, 3, and 7 after implantation by ICP-MS, plotted against the square root of the implantation period, $\sqrt{t}$. The ratios of Mg (d), Ca (e), and P (f) to insoluble salts weight are also plotted against $\sqrt{t}$.

by the higher concentration of released Mg^{2+} and higher local pH, which reduces the solubility of insoluble salts [33]. The concentration of released Mg^{2+} near the specimen surface is influenced by the diffusion rate in the microenvironment at the implantation site. The higher W_{inso}/W_{loss} at day 1 of the hematoma group may be attributed to its higher corrosion rate and less diffusive environment. The shift in W_{inso}/W_{loss} may reflects the change in the microenvironment in hematoma, such as recovery of microcirculation and decrease in local pH due to the retardation of Mg corrosion.

3.3. Elemental quantification of insoluble salts by inductively coupled plasma-mass spectroscopy

3.3.1. Magnesium

The Mg weight as insoluble salts was summarized in figure 3(a) and table S3 of the supplementary materials. A significant increase in Mg weight was observed over time for both groups ($F(1,5) = 21.416$, $p < 0.001$). Both groups displayed a similar increase rate of Mg weight ($p > 0.1$ by Parallelism test of 2 regression lines against the square root of the implantation period). However, the intercepts of the regression lines were significantly different ($p < 0.01$). This trend is similar to that of the insoluble salt weight as described in the previous chapter, indicating the significant difference was occurred in the very early stage of the implantation (within 24 h). The Mg weight of the hematoma group was significantly higher than that of the non-hematoma group on days 1 and 7.

The ratio of Mg weight to W_{inso} was plotted in figure 3(d), indicating its stability around 0.18 through days 1–7 for both groups. This agreement in Mg/W_{inso} also suggests that the same kinds of

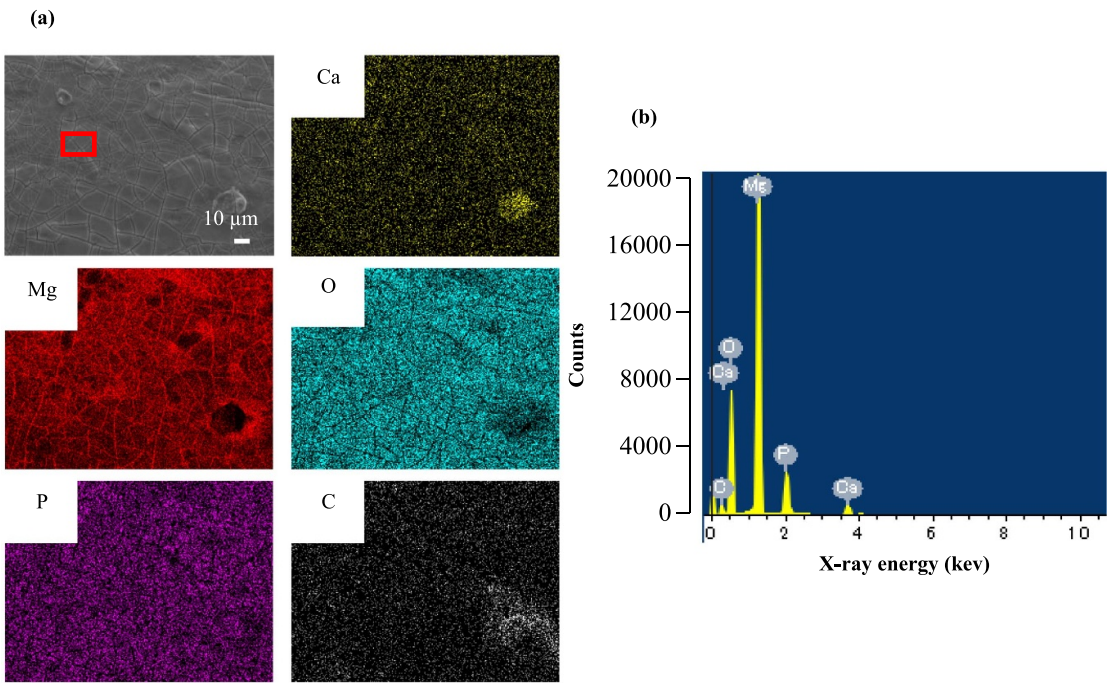

Figure 4. Typical examples of the EDX analysis for the top surface (a) of pure Mg specimen implanted for 1 d under non-hematoma condition. The EDX spectrum (b) was obtained by the point analysis of a red square indicated in the SEM image in (a).

insoluble salts containing Mg were formed on the specimen surface for both groups.

3.3.2. Calcium

The Ca weight as insoluble salts was summarized in figure 3(b) and table S4 in the supplementary materials. The hematoma group has a slightly larger increase rate of the Ca weight than the non-hematoma group, but no significant difference was observed between the two groups ($p > 0.1$ by the Parallelism Test of 2 regression lines). However, the intercepts of the regression lines were different ($p < 0.1$ by the Parallelism Test). This indicates that the hematoma group has the significantly smaller precipitation of Ca salts in the very early stage of implantation.

The ratio of Ca weight to W_{inso} was plotted in figure 3(e) against the square root of the implantation period. For the non-hematoma group, Ca/W_{inso} is significantly greater than that of the hematoma group at day 1. It decreased thereafter, whereas that of the hematoma group slightly increased. These data clearly indicate the different trend of Ca salt precipitation between non-hematoma and hematoma groups.

3.3.3. Phosphorus

The P weight as insoluble salts was summarized in figure 3(c) and table S5 in the supplementary materials. In the same manner to Ca, the hematoma group has a slightly larger increase rate of P weight than the other with no significance ($p > 0.1$ by the parallelism test of the regression lines), but a significant difference was observed in their intercepts ($p > 0.1$). As shown in figure 3(f), the non-hematoma group has the significantly greater P/W_{inso} than the other on days 1, 3, and 7. The P/W_{inso} of the non-hematoma group decreased from day 1–3, while that of the hematoma group slightly increased through the implantation period. These trends are similar to those of Ca, suggesting the co-precipitation of Ca and P on the specimen surface.

3.4. Surface analysis of implanted specimens by SEM-EDX

3.4.1. Non-hematoma group

Typical SEM-EDX images of the post-implantation specimen surface were shown in figure 4 (day 1), and supplementary figures S2 (day 3) and S3 (day 7) with those of the pre-implantation specimen surface (supplementary figure S1). A thin, homogeneous insoluble salt layer with shallow cracks was formed on the specimen surface on day 1. The distribution of Mg on the specimen surface became less pronounced on day 3, and the distribution of Ca and P was dominant on day 7. The formation of O, Ca, and P rich layer at specimen surface was confirmed by the cross-sectional analysis of a pure Mg wire implanted into a rat aorta wall [34], which agrees with the finding in this study. On the pre-implantation specimen, Mg was detected as the main peak with negligible peaks assigned to C, O, and P (figure S1).

The results of EDX point analysis are summarized in figure 5 and table S6 in the supplementary

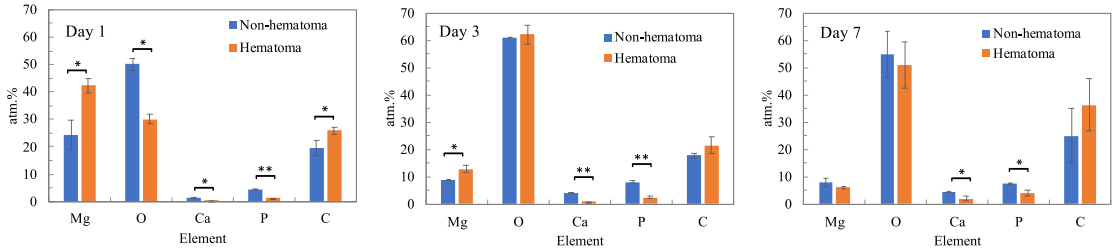

Figure 5. Results of quantitative EDX analysis of pure Mg specimens implanted under non-hematoma and hematoma conditions (atm. %) for day1(a), day 3(b), and day 7(c). The statistical significance between the groups was decided by *t*-test ($^{*}p < 0.05$, $^{**}p < 0.01$).

materials. It clearly shows the different pattern of elemental distributions at day 1 from those at day 3 and 7. The relatively high Mg concentration with low O concentration at day 1 indicates the formation of a thin insoluble salt layer on the specimen surface. At day 3 and 7, the Mg concentration decreased whereas Ca and P increased, suggesting the growth of the insoluble salt layer. At day 1, concentrations of Ca and P are much smaller than that of Mg, whereas those by ICP-MS analysis are close to that of Mg. This suggests that the EDX results includes the signals from the Mg substrate because the insoluble salt layer is thin as described. At day 3 and 7, the ratios of Ca and P to Mg increased to be close to 1, which is even larger than those by ICP-MS analysis. This indicates the higher distribution of Ca and P on the surface of the insoluble salt layer at day 3 and 7.

3.4.2. Hematoma group

Typical SEM-EDX images of the Mg specimen surface after implantation were shown in figure 6 (day 1), and supplementary figures S4 (day 3) and S5 (day 7). No crack was observed on the specimen surface on day 1 whereas shallow cracks were observed in the non-hematoma group. Moreover, the surface was generally uneven with bumps. On day 3, surface cracks were observed with a decrease in Mg, an increase in Ca and P distribution; this trend was further enhanced on day 7.

The results of EDX analysis are summarized in figure 5, and supplementary table S6 with those of the non-hematoma group. Similar to the non-hematoma group, the concentration of Mg decreased while those of Ca and P increased with the increase in the implantation period. On day 1, the hematoma group has 1.7 times higher Mg and 40% lower O than the other group, indicating the clear difference in the specimen surface composition between the two groups. Similar to the non-hematoma group, the relatively high Mg and low O concentration suggests the formation of a thin insoluble salt layer on the specimen surface. However, the hematoma group has the larger W_{inso} than the other (see figure 2(b)). This controversial result may be attributed to the inhomogeneity of insoluble salt formation on the specimen surface of the hematoma group, as observed in SEM images (figure 6(a)). These findings suggest that the hematomas strongly influence the insoluble salt precipitation at the initial stage of implantation. On day 3 and 7, the surface compositions of the hematoma group were similar to those of non-hematoma group, with significantly less Ca and P concentrations. Similar to the non-hematoma group, the ratios of Ca and P to Mg are larger than those by ICP-MS analysis, suggesting the higher distribution of it at the surface of the insoluble salt layer. In other words, Mg salts are formed in the deeper part of the insoluble salt layer on days 3 and 7. The concentration of C was increased from day 3 to day 7, suggesting the co-precipitation of organic compounds in the insoluble salt layer.

3.5. Analysis of the insoluble salts by micro-Raman spectroscopy

3.5.1. Raman spectra of the non-hematoma group

Typical Raman spectra of the specimens in the non-hematoma group are shown in figure 7 with their major peaks summarized in table 2. For reference, the Raman spectrum of the pre-immersion specimen is shown in the supplementary figure S6, which does not have a specific peak in the region of 1100–950 cm^{-1}.

On day 1, the peaks at 960 or 1085 cm^{-1} were detected at the different sites on the specimen surface. The peak at 960 cm^{-1} is attributed to the ν_1 stretching vibration of PO_4^{3-} [35, 36], while the peak at 1080–1090 cm^{-1} is attributed to the stretching vibration of CO_3^{2-} [37, 38], confirming local precipitation of phosphate and carbonate at the early stage of implantation. The detection of CO_3^{2-} and PO_4^{3-} on the implanted specimen surface was also reported by the microscopic Fourie transform infrared spectroscopy of the pure Mg wire surface implanted into the rat aorta wall [34, 39]. On day 3, peaks at 967 and 1083 cm^{-1}, assigned to PO_4^{3-} and CO_3^{2-}, were observed at the same site, suggesting the co-precipitation of phosphate and carbonate. On day 7, however, the peak corresponding to CO_3^{2-} disappeared while the peak assigned to PO_4^{3-}

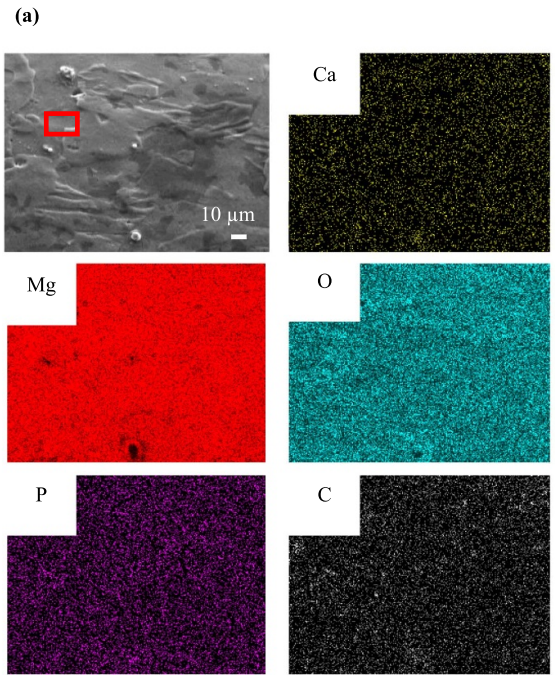

Figure 6. Typical examples of the EDX analysis for the top surface (a) of pure Mg specimen implanted for 1 d under hematoma condition. The EDX spectrum (b) was obtained by the point analysis of a red square indicated in the SEM image in (a).

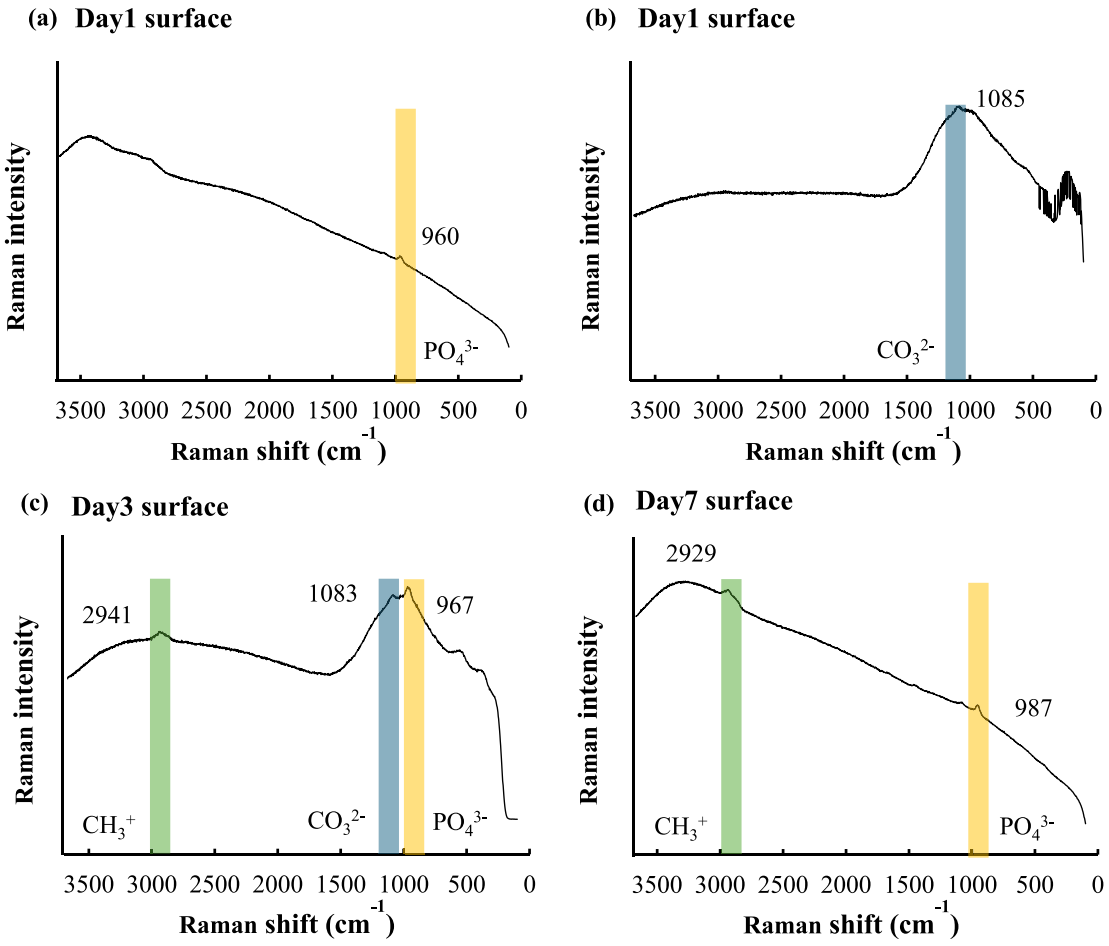

Figure 7. Raman spectra of the specimen surface in the non-hematoma group. (a) (b) Different sites on day 1, (c) day 3, and (d) day 7.

Table 2. Raman shifts of the major peaks observed for insoluble salts formed on the Mg specimen surface implanted under non-hematoma condition.

	Wavenumaber (cm^{-1})			
	PO_4^{3-}	CO_3^{2-}	CH_3^+	Appearance form
Day1	960	1085		Independently
Day3	967	1083	2941	Simultaneously
Day7	987		2929	Simultaneously

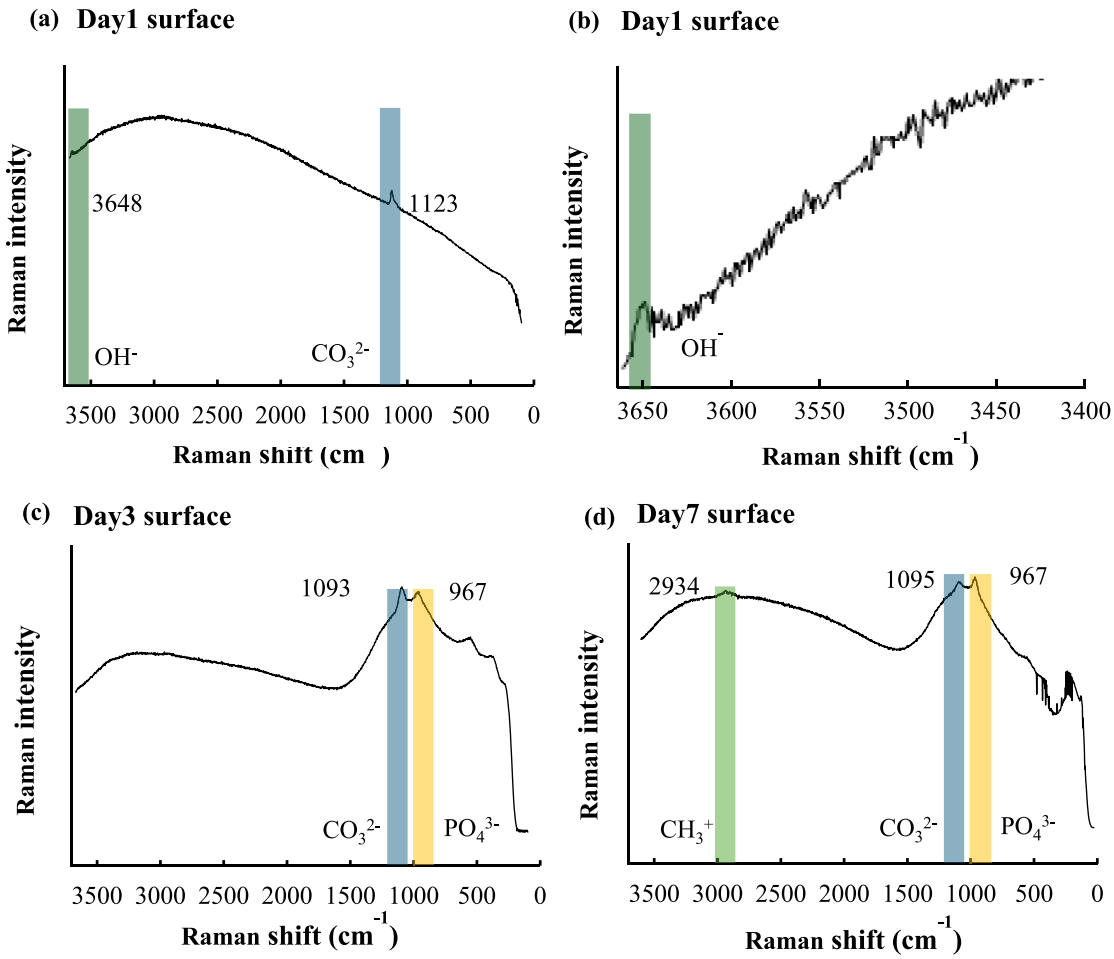

Figure 8. Raman spectra of the specimen surface in the hematoma group. (a) (b) Different sites on day 1, (c) day 3, and (d) day 7.

was observed at 987 cm^{-1}. This indicates the dominance of phosphate precipitation at day 7. On days 3 and 7, the peak at approximately 2930 cm^{-1} was also observed, which is attributed to the stretching vibration of CH_3^+ in organic substances [40, 41].

3.5.2. Raman spectra of the hematoma group

Typical Raman spectra of the specimens in the hematoma group were shown in figure 8 with their major peaks summarized in table 3. Peaks at 1123 and 3648 cm^{-1} were observed on day 1. Hydromagnesite, hydrated magnesium carbonate, has peaks corresponding to CO_3^{2-} and OH^- at 1120–1123 cm^{-1} and 3648 cm^{-1}, respectively [38]. Magnesium phosphate is another candidate; its Raman spectrum has a peak at 1122 cm^{-1} [42]. Therefore, hydromagnesite and/or magnesium phosphate may precipitate at the early stage of implantation, whereas carbonate and phosphate are observed on day 1 for the non-hematoma group. On day 3, peaks were observed at 967 and 1093 cm^{-1} whereas those at 967, 1095, and 2934 cm^{-1} were detected on day 7. These observations confirmed the co-precipitation of phosphate and carbonate on days 3 and 7 for the hematoma group, while only phosphate was observed on day 7 for the non-hematoma group. The co-precipitation or absorption of organic substances was also delayed

Table 3. Raman shifts of the major peaks observed for insoluble salts formed on the Mg specimen surface implanted under hematoma condition.

	Wavenumaber (cm^{-1})					
	PO_4^{3-}	PO_4^{3-} or CO_3^{2-}	CO_3^{2-}	CH_3^+	OH^-	Appearance form
Day1		1123			3648	Simultaneously
Day3	967		1093			Simultaneously
Day7	967		1095	2934		Simultaneously

for the hematoma group; which was observed from day 3 for the non-hematoma group.

4. Discussion

Many reports describe the degradation behavior of Mg and its alloys, both *in vitro* and *in vivo*; however, they have different results in degradation rates and structures of the insoluble salt layer formed on the specimen surface [13, 43, 44]. In *in-vitro* studies, the corrosion of Mg depends on the chemical composition and pH of the immersion solution [8], in which Mg^{2+}, OH^- and H_2 gas diffuse easily. However, when implanted *in vivo*, the degradation behavior is further complicated; because multiple factors are involved, including relatively high ionic strength, ion/gas diffusion by blood flow, cellular influence, and the presence of organic compounds such as glucose, amino acids, and proteins [45]. The corrosion behavior of implanted Mg specimen is more complex because surgical invasion and bleeding from the fracture site markedly affect the environment of the implantation site compared with that in normal tissue.

In case of the specimen implantation into normal tissue with reasonable bleeding control, an interstitial fluid will contact to the specimen surface. This fluid has a buffering ability to maintain its pH of 6.60–7.60, however, it is more variable than the pH of blood [46]. In addition to chloride ion (Cl^-), it contains HCO_3^- and HPO_4^{2-} which contribute to pH buffering in an equilibrium state [47, 48]. As components of the interstitial fluid penetrate through lymphatic vessels and capillary walls to circulate in the whole body, the Mg^{2+} and OH^- released by Mg corrosion are expected to diffuse relatively quickly by microcirculation. Even so, the pH of the interstitial fluid near the specimen surface can locally increase, depending on the corrosion rate of Mg specimen, buffering ability of the fluid, and diffusion condition in the microenvironment as observed in the *in vitro* experiments [11, 49]. Then, the concentrations of CO_3^{2-}, HPO_4^{2-}, and PO_4^{3-} increase, resulting in the reaction of these ions with Mg^{2+} and Ca^{2+} in the interstitial fluid to form insoluble salts as $MgCO_3$, $Mg_3(PO_4)_2$, $CaCO_3$, and $Ca_3(PO_4)_2$ in addition to $Mg(OH)_2$ [10, 50]. These insoluble salts precipitate and cover the specimen surface, retarding the corrosion rate.

In clinical cases, unexpected bleeding from fracture surfaces or soft tissue after the surgery creates the microenvironment different from that in the interstitial fluid. Hematomas cause primary hemostasis via platelet aggregation, followed by an accelerated coagulation cascade and fibrin accumulation to form a fibrin network, resulting in an aggregate isolated from the surrounding environment [51, 52]. The loss of capillary and circulation inside the hematoma reduces the oxygen supply, resulting in high concentrations of lactic acid by anaerobic metabolism and CO_2 exudation from dead cells [19, 53]. However, the gradual gathering of endothelial cells forms capillaries, and consequently resumes circulation and diffusion within the hematoma [54]. Thus, the pH within the hematoma drops to approximately 5.0 and recovers around pH 7.0 over about two weeks [18, 19, 55]. This low-pH, low-circulation microenvironment in the hematomas can be an accelerating factor for the corrosion of the implanted Mg specimen. There are a few *in vitro* studies investigating the effect of whole blood on Mg alloy corrosion for short time as 6 h [28, 29], but no *in vivo* study was performed to investigate the effect of hematoma on the corrosion behavior of Mg or Mg alloy specimens so far.

In this study, pure Mg specimens were implanted into rat thighs under hematoma or non-hematoma conditions up to 7 d. The volume of the hematoma formed at the implantation site is estimated 200 mm^3, which is equivalent to 20–30 ml hemorrhage for a human adult weighing 60 kg. This volume is an acceptable level in the clinical cases of fracture fixation as unexpected bleeding after surgery.

The specimens were collected after the designated period of implantation, followed by weight loss measurement and quantification of Mg, Ca, and P in insoluble salts by ICP-MS. The elemental distributions and chemical structures of the insoluble salts formed on the specimen surface were analyzed by SEM-EDX and Raman spectroscopy. As the results, the hematoma accelerated the corrosion of pure Mg with changes in the structure of the insoluble salt layer. The corrosion rate estimated by the weight loss for the hematoma group was almost doubled that for the non-hematoma group after 7 d of implantation (figure 2(a)). Wang *et al* reported that the pure Mg wire implanted into rat aorta lumen was slightly less corroded than that

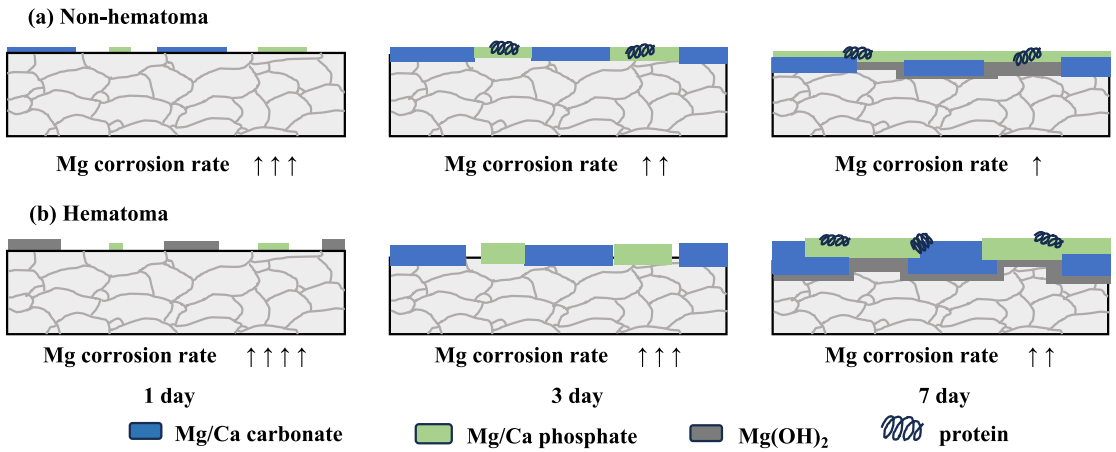

Figure 9. Mechanism of insoluble salt formation. The non-hematoma group (a) and the hematoma group (b).

implanted in aorta wall [39], which is controversial to that obtained in this study. In their study, the specimen implanted into aorta lumen was initially exposed to the dynamic blood flow but was eventually covered by a fibrous capsule before 3 d [39]. This suggests the difference in the microenvironment between the aorta lumen and the hematoma in the present study. Initial non-dynamic, fibrous structure of hematoma may accelerate the corrosion rate of Mg specimen than in non-hematoma tissue. The shift in W_{inso}/W_{loss} of the hematoma group with the increase in the implantation period indicates the change in the microenvironment influencing the insoluble salt precipitation, which may correspond to the resume of microcirculation.

The ICP-MS and EDX analysis revealed the difference in the insoluble salt precipitation between the hematoma and non-hematoma groups. The EDX analysis found that the hematoma group had the significantly lower concentrations of Ca and P than those of the non-hematoma group (figure 5 and table S2). In comparison to the results by ICP-MS, Ca and P tended to distribute at the surface of the insoluble salt layer on days 3 and 7. Raman spectroscopy confirmed that the non-hematoma group had a phosphate layer on the specimen surface from the early stage of implantation, while the hematoma group had a less or delayed formation of it. In the latter group, carbonate is more dominant than phosphate, and hydroxide was observed on day 1.

Differences in structures of the insoluble salt layer between the hematoma and non-hematoma groups are possibly attributed to the difference in pH, ion supply, and diffusion in the microenvironment [10]. The schematic illustrations of the insoluble salt precipitation processes are shown in figure 9. At the very initial moment of the implantation, the local concentrations of Mg^{2+} and OH^- increased near the specimen surface due to a corrosion reaction. This guides to temporal precipitation of $Mg(OH)_2$, which eventually disappears when the pH is lower than 11.5 [3]. Instead, precipitation of $MgCO_3$ likely occurs since HCO_3^- is abundant in the interstitial fluid. In the non-hematoma group, Mg^{2+} and OH^- diffuse relatively quickly with supplies of Ca^{2+} and PO_4^{3-} by microcirculation, leading to precipitation of calcium phosphate even at the early stage of implantation as day 1. Under non-hematoma condition, this calcium phosphate formation at the early phase of implantation may efficiently retard the corrosion of the Mg specimen.

In the hematoma group, however, the lower pH in hematomas induces initial rapid corrosion of the Mg specimen, which results in the higher local pH at the specimen surface. This leads to the larger amount of $Mg(OH)_2$ precipitation than the other condition, as detected by Raman spectroscopy on day 1. Furthermore, low ion diffusion with low Ca^{2+} and PO_4^{3-} supplies in the hematomas guided to hydromagnesite precipitation at the early stage of implantation. Eventually, the carbonate becomes dominant along with the progress of fibrinolysis. The precipitation of calcium phosphate delays to day 3 and thereafter, which may be one of the causes of the higher corrosion rate of Mg specimen under hematoma condition.

The fibrinolysis as well as the recovery process of hematomas may influence the microenvironment and thus insoluble salt precipitation on the implanted specimen surface. In the hematoma group, both Ca and P ratios against W_{inso} increased with the increase in implantation period (figures 3(e) and (f)) while W_{inso}/W_{loss} decreased (figure 2(c)). These trends may reflect the recovery of local pH at the specimen surface in the hematoma along with the decrease in the corrosion rate of the Mg specimen.

The insoluble salts layer formed on the specimen surface at the early stage of implantation can

influence the following tissue reaction against the specimen. The formation of a stable calcium phosphate layer on the Mg alloy specimen at the early stage of implantation is beneficial for bone formation [56]. Mg-based device with localized contact to the hematoma may have localized corrosion, potentially leading to its unintended failure [57]. Unintended breakage of the implanted device fails to achieve the expected bone fusion, which causes fistula formation and soft tissue damage leading to prolonged inflammation [58]. The results obtained in this paper indicate the hematoma as an acceleration factor for the corrosion of Mg-based devices. That means, the Mg-based devices need to be designed and developed with the consideration of hemorrhage and hematoma risks at the implantation site. It also suggests the importance of the optimization of surgical procedures to control the hemorrhage at implantation and to reduce the unexpected bleeding after the surgery.

A limitation of the present study is that the hematoma was formed via a small bony foramen; the microenvironment in the hematoma may be different from that formed via soft tissues or fracture surfaces. In the general implantation condition for bone fracture fixation, the bone marrow was also exposed to the fixture device to some extent, leading to suppression of Ca and P supply due to demineralization in bone marrow. In this study, implantation tests were conducted as the entire specimen was inserted into a hematoma. However, we believe that hematoma can accelerate localized corrosion even with its partial contact to the specimen surface. *In vivo* experiments of a specimen having a similar shape to clinical devices are recommended for the accurate evaluation of the effect of hemorrhage in clinical conditions.

5. Conclusion

In this study, the corrosion behavior of pure Mg was investigated during the early stages of *in-vivo* implantation under hematoma and non-hematoma conditions. As the results, hematoma promotes the corrosion of the Mg specimen, influencing the structure of the insoluble salt layer formed on the specimen surface. These effects were attributed to the microenvironment in hematoma; lower pH and less microcirculation. Obtained results indicate the risk of hematoma by unexpected bleeding after implant surgery that accelerates the corrosion of Mg-based devices leading to their failure in fracture fixation. It also suggests the importance of considering the risk of hematoma on the development and design of new Mg-based fixtures.

Data availability statement

All data that support the findings of this study are included within the article (and any supplementary files).

Acknowledgments

We thank Ms. Miho Oikawa of the Technical Division of Tohoku University Graduate School of Dentistry and Ms. Yoko Nakano, Mr. Takuya Takanashi, and Mr. Syunsuke Kayamori of the Technical Division of Tohoku University Graduate School of Engineering for their technical support

Conflict of interest

This study was funded by Nihon Parkerizing Co., Ltd.

Funding statement

Part of this research was supported by Grants-in-Aid for Scientific Research (issue numbers 22H03988, K23K159480, and S23310203) from the Japan Society for Promotion of Science.

ORCID iDs

Yu Yusa https://orcid.org/0009-0009-1395-8182
Takayuki Aizawa https://orcid.org/0000-0002-6231-0368

References

[1] Niranjan C A *et al* 2023 Magnesium alloys as extremely promising alternatives for temporary orthopedic implants—A review *J. Magnes. Alloy* **11** 2688–718
[2] Jing X, Ding Q, Wu Q, Su W, Yu K, Su Y, Ye B, Gao Q, Sun T and Guo X 2021 Magnesium-based materials in orthopaedics: material properties and animal models *Biomater. Transl.* **2** 197–213
[3] Xing F, Li S, Yin D, Xie J, Rommens P M, Xiang Z, Liu M and Ritz U 2022 Recent progress in Mg-based alloys as a novel bioabsorbable biomaterials for orthopedic applications *J. Magnes. Alloy* **10** 1428–56
[4] Azadani M N, Zahedi A, Bowoto O K and Oladapo B I 2022 A review of current challenges and prospects of magnesium and its alloy for bone implant applications *Prog. Biomater.* **11** 1–26
[5] Feliu S, Maffiotte C, Samaniego A, Galván J C and Barranco V 2011 Effect of naturally formed oxide films and other variables in the early stages of Mg-alloy corrosion in NaCl solution *Electrochim. Acta* **56** 4554–65
[6] Wang L *et al* 2022 Review: degradable magnesium corrosion control for implant applications *Materials* **15** 6197
[7] Johnston S, Shi Z and Atrens A 2015 The influence of pH on the corrosion rate of high-purity Mg, AZ91 and ZE41 in bicarbonate buffered Hanks' solution *Corros. Sci.* **101** 182–92
[8] Ng W F, Chiu K Y and Cheng F T 2010 Effect of pH on the in vitro corrosion rate of magnesium degradable implant material *Mater. Sci. Eng.* C **30** 898–903
[9] Inoue H, Sugahara K, Yamamoto A and Tsubakino H 2002 Corrosion rate of magnesium and its alloys in buffered chloride solutions *Corros. Sci.* **44** 603–10
[10] Gonzalez J, Hou R Q, Nidadavolu E P S, Willumeit-Römer R and Feyerabend F 2018 Magnesium degradation under physiological conditions—Best practice *Bioact. Mater.* **3** 174–85
[11] Lamaka S V, Gonzalez J, Mei D, Feyerabend F, Willumeit-Römer R and Zheludkevich M L 2018 Local pH and its evolution near Mg alloy surfaces exposed to simulated body fluids *Adv. Mater. Interfaces* **5** 1800169

[12] Witecka A, Bogucka A, Yamamoto A, Máthis K, Krajňák T, Jaroszewicz J and Święszkowski W 2016 In vitro degradation of ZM21 magnesium alloy in simulated body fluids *Mater. Sci. Eng.* C **65** 59–69
[13] Yamamoto A and Hiromoto S 2009 Effect of inorganic salts, amino acids and proteins on the degradation of pure magnesium in vitro *Mater. Sci. Eng.* C **29** 1559–68
[14] Zhao D, Witte F, Lu F, Wang J, Li J and Qin L 2017 Current status on clinical applications of magnesium-based orthopaedic implants: a review from clinical translational perspective *Biomaterials* **112** 287–302
[15] Wichelhaus A, Emmerich J and Mittlmeier T 2016 A case of implant failure in partial wrist fusion applying magnesium-based headless bone screws *Case Rep. Orthop.* **2016** 7049130
[16] Miura C *et al* 2016 In vivo corrosion behaviour of magnesium alloy in association with surrounding tissue response in rats *Biomed. Mater.* **11** 025001
[17] Maruyama M, Rhee C, Utsunomiya T, Zhang N, Ueno M, Yao Z and Goodman S B 2020 Modulation of the inflammatory response and bone healing *Front. End.* **11** 386
[18] Wray J B 1970 The biochemical characteristics of the fracture hematoma in man *Surg. Gynecol. Obstet.* **130** 847–52
[19] Walters G, Pountos I and Giannoudis P V 2018 The cytokines and micro-environment of fracture haematoma: current evidence *J. Tissue Eng. Regen. Med.* **12** e1662–77
[20] Kolar P *et al* 2011 Human early fracture hematoma is characterized by inflammation and hypoxia *Clin. Orthop. Relat. Res.* **469** 3118-26
[21] Silver I A, Murrills R J and Etherington D J 1988 Microelectrode studies on the acid microenvironment beneath adherent macrophages and osteoclasts *Exp. Cell Res.* **175** 266–76
[22] Girard A, Lopez C D, Chen J, Perrault D, Desai N, Bruckman K C, Bartlett S P and Yang R 2022 Epistaxis after orthognathic surgery: literature review and three case studies *Craniomaxillofac. Trauma Reconstr.* **15** 147–63
[23] Plaass C *et al* 2016 Early results using a biodegradable magnesium screw for modified chevron osteotomies *J. Orthop. Res.* **34** 2207–14
[24] Sukotjo C, Lima-Neto T J, Santiago Júnior J F, Faverani L P and Miloro M 2020 Is there a role for absorbable metals in surgery? A systematic review and meta-analysis of Mg/Mg alloy based implants *Materials* **13** 3914
[25] Cho D H, Avey T, Nam K H, Dean D and Luo A A 2022 *In vitro* and *in vivo* assessment of squeeze-cast Mg-Zn-Ca-Mn alloys for biomedical applications *Acta Biomater.* **150** 442–55
[26] Elkaiam L, Hakimi O, Yosafovich-Doitch G, Ovadia S and Aghion E 2020 *In vivo* Evaluation of Mg-5%Zn-2%Nd alloy as an innovative biodegradable implant material *Ann. Biomed. Eng.* **48** 380–92
[27] Tie D, Guan R, Liu H, Cipriano A, Liu Y, Wang Q, Huang Y and Hort N 2016 An in vivo study on the metabolism and osteogenic activity of bioabsorbable Mg-1Sr alloy *Acta Biomater.* **29** 455–67
[28] Geis-Gerstorfer J, Schille C, Schweizer E, Rupp F, Scheideler L, Reichel H-P, Hort N, Nolte A and Wendel H-P 2011 Blood triggered corrosion of magnesium alloys *Mater. Sci. Eng.* B **176** 1761–6
[29] Feyerabend F, Wendel H-P, Mihailova B, Heidrich S, Agha N A, Bismayer U and Willumeit-Römer R 2015 Blood compatibility of magnesium and its alloys *Acta Biomater.* **25** 384–94
[30] Hafeez M A, Farooq A, Zang A, Saleem A and Deen K M 2020 Phosphate chemical conversion coatings for magnesium alloys: a review *J. Coat. Technol. Res.* **17** 827–49
[31] Hino M, Murakami K and Kanadani K 2013 Pretreatment for magnesium alloy *J. Surf. Finish. Soc. Jpn.* **64** 650–5
[32] Chen S, Tan L, Zhang B, Xia Y, Xu K and Yang K 2017 *In vivo* study on degradation behavior and histologic response of pure magnesium in muscles *J. Mater. Sci. Technol.* **33** 469–74
[33] Hayashi M, Yamamoto A, Aizawa T, Yusa Y, Shimizu Y and Imai Y 2024 In vitro analysis of insoluble salt formation mechanism associated with Mg corrosion—variations depending on the diffusion environment in model tissue *Biomed. Mater.* **19** 025010
[34] Bowen P K, Drelich J and Goldman J 2014 Magnesium in the murine artery: probing the products of corrosion *Acta Biomater.* **10** 1475–83
[35] Stammeier J A, Purgstaller B, Hippler D, Mavromatis V and Dietzel M 2018 In-situ Raman spectroscopy of amorphous calcium phosphate to crystalline hydroxyapatite transformation *Methods X* **5** 1241–50
[36] Karampas I A and Kontoyannis C G 2013 Characterization of calcium phosphates mixtures *Vib. Spectrosc.* **64** 126–33
[37] Kuenzel C, Zhang F, Ferrándiz-Mas V, Cheeseman C R and Gartner E M 2018 The mechanism of hydration of MgO-hydromagnesite blends *Cem. Concr. Res.* **103** 123–9
[38] Schmid T, Kraft R and Dariz P 2021 Shedding light onto the spectra of lime—Part 2: raman spectra of Ca and Mg carbonates and the role of d-block element luminescence *J. Raman Spectrosc.* **52** 1462–72
[39] Wang J *et al* 2017 *Ex vivo* blood vessel bioreactor for analysis of the biodegradation of magnesium stent models with and without vessel wall integration *Acta Biomater.* **50** 546–55
[40] Wang M, Cai Y, Zhao B and Zhu P 2017 Time-resolved study of nanomorphology and nanomechanic change of early-stage mineralized electrospun poly(lactic acid) fiber by scanning electron microscopy, Raman spectroscopy and atomic force microscopy *Nanomaterials* **7** 223
[41] Rygula A, Majzner K, Marzec K M, Kaczor A, Pilarczyk M and Baranska M 2013 Raman spectroscopy of proteins: a review *J. Raman Spectrosc.* **44** 1061–76
[42] Hilger D M, Hamilton J G and Peak D 2020 The influences of magnesium upon calcium phosphate mineral formation and structure as monitored by x-ray and vibrational spectroscopy *Soil Syst.* **4** 8
[43] Zeller-Plumhoff B, Tolnai D, Wolff M, Greving I, Hort N and Willumeit-Römer R 2021 Utilizing synchrotron radiation for the characterization of biodegradable magnesium alloys—From alloy development to the application as implant material *Adv. Eng. Mater.* **23** 2100197
[44] Sanchez A H M, Luthringer B J C, Feyerabend F, Willumeit R, Wang M, Cai Y, Zhao B and Zhu P 2015 Mg and Mg alloys: how comparable are in vitro and in vivo corrosion rates? A review *Acta Biomater.* **13** 16–31
[45] Saad A P M, Jasmawati N, Harun M N, Abdul Kadir M R, Nur H, Hermawan H and Syahrom A 2016 Dynamic degradation of porous magnesium under a simulated environment of human cancellous bone *Corros. Sci.* **112** 495–506
[46] Marunaka Y 2015 Roles of interstitial fluid pH in diabetes mellitus: glycolysis and mitochondrial function *World J. Diabetes* **6** 125–35
[47] Mueller W D, Nascimento M L and Lorenzo de Mele M F 2010 Critical discussion of the results from different corrosion studies of Mg and Mg alloys for biomaterial applications *Acta Biomater.* **6** 1749–55
[48] Seifter J L 2019 Body fluid compartments, cell membrane ion transport, electrolyte concentrations, and acid-base balance *Semin. Nephrol.* **39** 368–79
[49] Gonzalez J, Lamaka S V, Mei D, Scharnagl N, Feyerabend F, Zheludkevich M L and Willumeit-Römer R 2021 Mg biodegradation mechanism deduced from the local surface environment under simulated physiological conditions *Adv. Healthcare Mater.* **10** e2100053
[50] Kamrani S and Fleck C 2019 Biodegradable magnesium alloys as temporary orthopaedic implants: a review *Biometals* **32** 185–93
[51] Yang Y and Xiao Y 2020 Biomaterials regulating bone hematoma for osteogenesis *Adv. Healthcare Mater.* **9** e2000726
[52] Jambor C, Reul V, Schnider T W, Degiacomi P, Metzner H and Korte W C 2009 In vitro inhibition of factor XIII retards clot formation, reduces clot firmness, and increases fibrinolytic effects in whole blood *Anesth. Anal.* **109** 1023–8

[53] Khan M A 2015 *Textbook of Fractures and Dislocations* (Xlibris AU)
[54] Shiu H T, Leung P C and Ko C H 2018 The roles of cellular and molecular components of a hematoma at early stage of bone healing *J. Tissue Eng. Regen. Med.* **12** e1911–25
[55] Eliaz N 2012 *Degradation of Implant Materials* 1st edn (Springer)
[56] Gomes P S, Zomorodian A, Kwiatkowski L, Lutze R, Balkowiec A, Colaço B, Pinheiro V, Fernandes J C S, Montemor M F and Fernandes M H 2016 In vivo assessment of a new multifunctional coating architecture for improved Mg alloy biocompatibility *Biomed. Mater.* **11** 045007
[57] Zhao S *et al* 2023 A review of magnesium corrosion in bio-applications: mechanism, classification, modeling, *in-vitro*, and *in-vivo* experimental testing, and tailoring Mg corrosion rate *J. Mater. Sci.* **58** 12158–81
[58] Pisecky L, Luger M, Klasan A, Gotterbarm T, Klotz M C and Hochgatterer R 2021 Bioabsorbable implants in forefoot surgery: a review of materials, possibilities and disadvantages *EFORT Open Rev.* **6** 1132–9